A Sub-Nanostructural Transformable Nanozyme for Tumor Photocatalytic Therapy

Xi Hu[1,2,3], Nan Wang[1], Xia Guo[1], Zeyu Liang[1,4], Heng Sun[1], Hongwei Liao[1], Fan Xia[1], Yunan Guan[1], Jiyoung Lee[1,5], Daishun Ling[1,2,4] ✉, Fangyuan Li[1,4] ✉

HIGHLIGHTS

- An internal sub-nanostructural transformation of sub-nanostructural transformable gold@ceria (STGC-PEG) is initiated by the conversion between CeO_2 and electron-rich state of CeO_{2-x}, and active oxygen vacancies generation via the hot-electron injection from gold to ceria.

- The sub-nanostructural transformation of STGC-PEG enhances the peroxidase-like activity and activates the plasmon-promoted oxidase-like activity, resulting in an augmented reactive oxygen species output.

- STGC-PEG successfully achieves excellent low power (50 mW cm^{-2}) near-infrared light-activated photocatalytic ablation of tumors in vivo.

ABSTRACT The structural change-mediated catalytic activity regulation plays a significant role in the biological functions of natural enzymes. However, there is virtually no artificial nanozyme reported that can achieve natural enzyme-like stringent spatiotemporal structure-based catalytic activity regulation. Here, we report a sub-nanostructural transformable gold@ceria (STGC-PEG) nanozyme that performs tunable catalytic activities via near-infrared (NIR) light-mediated sub-nanostructural transformation. The gold core in STGC-PEG can generate energetic hot electrons upon
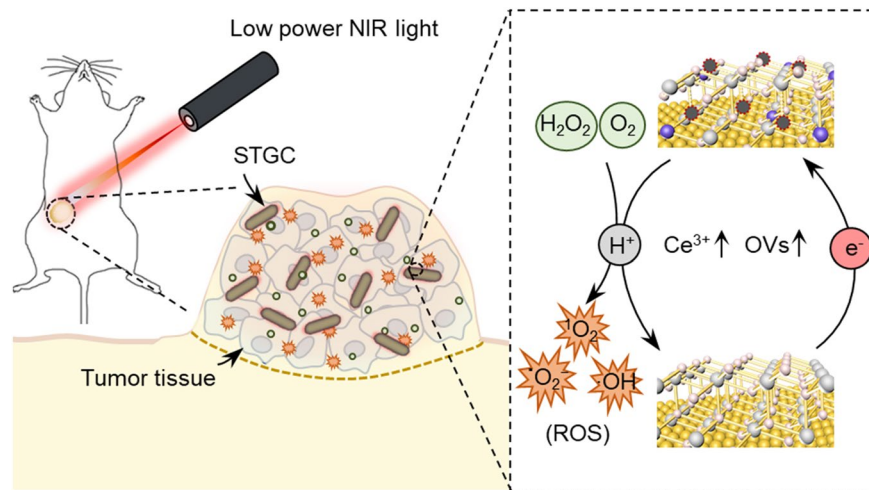
Xi Hu, Nan Wang, Xia Guo, and Zeyu Liang have contributed equally to this work.

✉ Daishun Ling, dsling@sjtu.edu.cn; Fangyuan Li, lfy@zju.edu.cn

1 Institute of Pharmaceutics, Hangzhou Institute of Innovative Medicine, College of Pharmaceutical Sciences, Zhejiang University, Hangzhou 310058, People's Republic of China

2 Frontiers Science Center for Transformative Molecules, State Key Laboratory of Oncogenes and Related Genes, School of Chemistry and Chemical Engineering, National Center for Translational Medicine, Shanghai Jiao Tong University, Shanghai 200240, People's Republic of China

3 Department of Clinical Pharmacy, The First Affiliated Hospital, Zhejiang University School of Medicine, Hangzhou 310003, People's Republic of China

4 WLA Laboratories, Shanghai 201203, People's Republic of China

5 Department of Biomedical-Chemical Engineering, The Catholic University of Korea, 43 Jibong-ro, Wonmi-gu, Bucheon-Si, Gyeonggi-do 14662, Republic of Korea

NIR irradiation, wherein an internal sub-nanostructural transformation is initiated by the conversion between CeO_2 and electron-rich state of CeO_{2-x}, and active oxygen vacancies generation via the hot-electron injection. Interestingly, the sub-nanostructural transformation of STGC-PEG enhances peroxidase-like activity and unprecedentedly activates plasmon-promoted oxidase-like activity, allowing highly efficient low-power NIR light (50 mW cm^{-2})-activated photocatalytic therapy of tumors. Our atomic-level design and fabrication provide a platform to precisely regulate the catalytic activities of nanozymes via a light-mediated sub-nanostructural transformation, approaching natural enzyme-like activity control in complex living systems.

KEYWORDS Nanozymes; Sub-nanostructural transformation; Catalytic activity; Reactive oxygen species; Photocatalytic therapy

1 Introduction

Enzymes, as powerful biocatalysts, have been widely used in biomedical research due to their high catalytic activities and substrate specificity [1, 2]. Though promising, the difficulties in storage and recycling, low chemical durability, and high cost of natural enzymes have limited their broad applications [3]. In recent years, artificial nanozymes with natural enzyme-mimetic activities have been developed [4–10], which attracted remarkable attention for various biomedical applications including biosensing, cytoprotection, tumor therapy, etc. [11–14]. However, different from natural enzymes, these artificial nanozymes generally lack stringent spatiotemporal structure regulation for a controllable catalytic activity in vivo, thus being undeniably far less efficient than natural enzymes [3, 15]. Up to date, tremendous efforts have been devoted to regulating the catalytic activities of nanozymes [11, 15–21]. The introduction of photo-sensitive functional ligands represents a major approach [11, 15–17]. For instance, based on the ultraviolet (UV) light-driven trans–cis isomerization of the azobenzene groups, imparting nanozymes with azobenzene containing surface ligands could selectively turn on their catalytic activity in a light-controlled manner [11, 15–17]. Unfortunately, the limited tissue penetration depth and genotoxicity of UV light as well as indirect structure regulation-based activity control restrict their further in vivo applications [22]. Self-assembly/disassembly remains another approach to tuning the enzymatic activities of nanozymes via controlled sequestering/exposing of their surface catalytic sites, which, however, lacks the spatiotemporal controllability in harsh biological microenvironments [11, 17–20].

In living systems, the regulation of catalytic activities of natural enzymes generally depends on the dynamic rearrangement of their intrinsic structures [23–25]. For instance, chymotrypsinogen can be activated by trypsin-mediated cleavage of peptide bonds between Arg15 and Ile16 [26],

and DNA photolyase would undergo a concerted structural change during photoactivation to initiate the repair of the impaired duplex [27]. The structural reconfiguration-mediated regulation of enzymatic activities is essential to the coordination of numerous biochemical events in living systems [24, 28, 29], which may represent the ultimate and yet to be implemented strategy to endow nanozymes with natural enzyme-like regulatability.

Inspired by nature, we herein propose a photon-driven sub-nanostructural transformable nanozyme that performs tunable catalytic activities via intrinsic sub-nanostructural transformation. Plasmonic metal nanomaterials (e.g., Au, Ag nanostructures) have a unique surface plasmon resonance (SPR) effect and can generate energetic hot electrons upon resonant light excitation [30–33]. Particularly, when coupled with semiconducting nanomaterials (e.g., CeO_2, TiO_2 nanostructures), the electronic properties of the conjoined nanomaterials can be further exploited through the direct plasmon-excited electron transfer, thus boosting their photocatalytic performances [34–36]. Consequently, the designed integration of plasmonic metal/semiconductor nanostructures is anticipated to achieve the photon-driven sub-nanostructural transformation via regulating their electronic properties to initiate the local atomic reconstruction [37, 38], so as to facilitate the catalytic activity regulation of nanozymes.

To prove our concept, a sub-nanostructural transformable gold@ceria (STGC) nanozyme was synthesized by controlled assembly of ultrafine ceria nanoparticles (CeO_2 NPs) onto the plasmonic gold nanorods (GNRs), which provides strong near-infrared (NIR) light absorption and abundant surface reactive sites for efficient catalytic reactions [39]. Unprecedentedly, once triggered by 808 nm irradiation, plasmon-excited hot electrons directly transferred from Au to CeO_2, converting CeO_2 to electron-rich state of CeO_{2-x} and inducing the generation of active oxygen vacancies (OVs) to dynamically reconstruct the
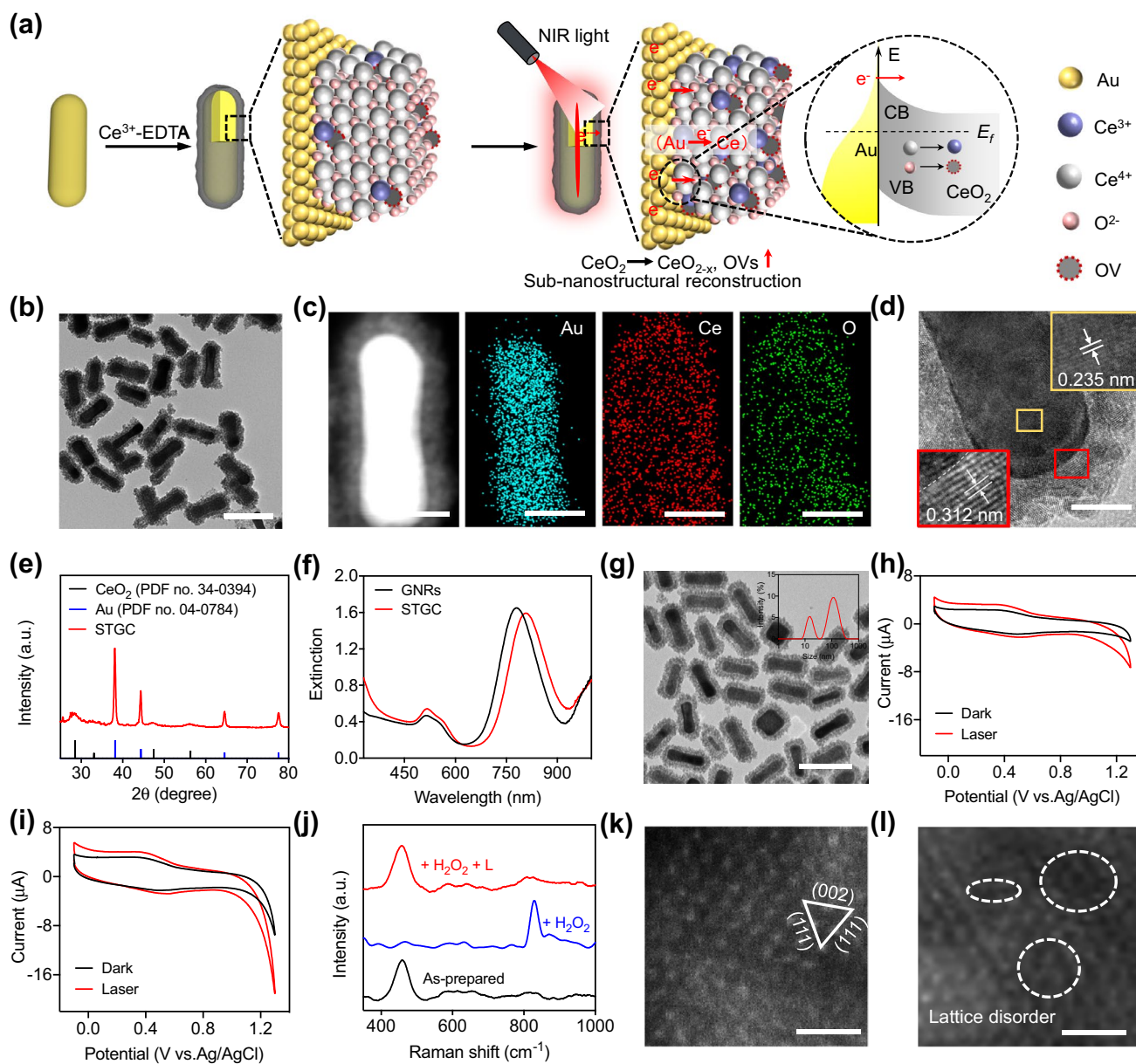
Fig. 1 Design and characterization of photon-driven sub-nanostructural transformable nanozymes. **a** Schematic illustration of the design and photon-driven sub-nanostructural transformation of STGC through the direct electron transfer. Once triggered by near-infrared (NIR) irradiation, plasmon-excited hot electrons directly transfer from Au to CeO_2, thus converting CeO_2 to electron-rich state of CeO_{2-x}, and producing active oxygen vacancies (OVs) to dynamically reconstruct the sub-nanostructure of STGC. **b** TEM image of STGC. Scale bar, 100 nm. **c** HAADF-STEM image of a single STGC and the corresponding elemental mapping. Scale bar, 20 nm. **d** HRTEM images of STGC. Scale bar, 10 nm. **e** XRD pattern of STGC. **f** UV–Vis absorption of GNRs and STGC. The LSPR peak of GNRs red shifts from 781 to 807 nm after CeO_2 coating. **g** TEM image of PEGylated STGC (STGC-PEG). Inset: hydrodynamic diameter distribution of STGC-PEG. Scale bar, 100 nm. **h, i** Cyclic voltammograms of STGC (black line) and STGC+laser (red line, 808 nm) without (**h**) and with H_2O_2 treatment (**i**). **j** Raman spectra of STGC after different treatments (L denotes laser) ($\lambda_{ex}=488$ nm). **k, l** HAADF-STEM images of STGC treated with H_2O_2 before (**k**) and after (**l**) 808 nm laser irradiation. The O-related defect induced lattice disorder is indicated by the dashed circles. Scale bar, 1 nm

sub-nanostructure of STGC-PEG (Fig. 1a). Such an internal sub-nanostructural transformation ingeniously regulated the peroxidase (POD)- and oxidase (OXD)-like catalytic activities of STGC-PEG for reactive oxygen species

(ROS) generation, enabling highly efficient photocatalytic therapy (PCT) of tumors. The as-designed sub-nanostructural transformable STGC-PEG represents a proof-of-concept of natural enzyme-like catalytic activity regulation
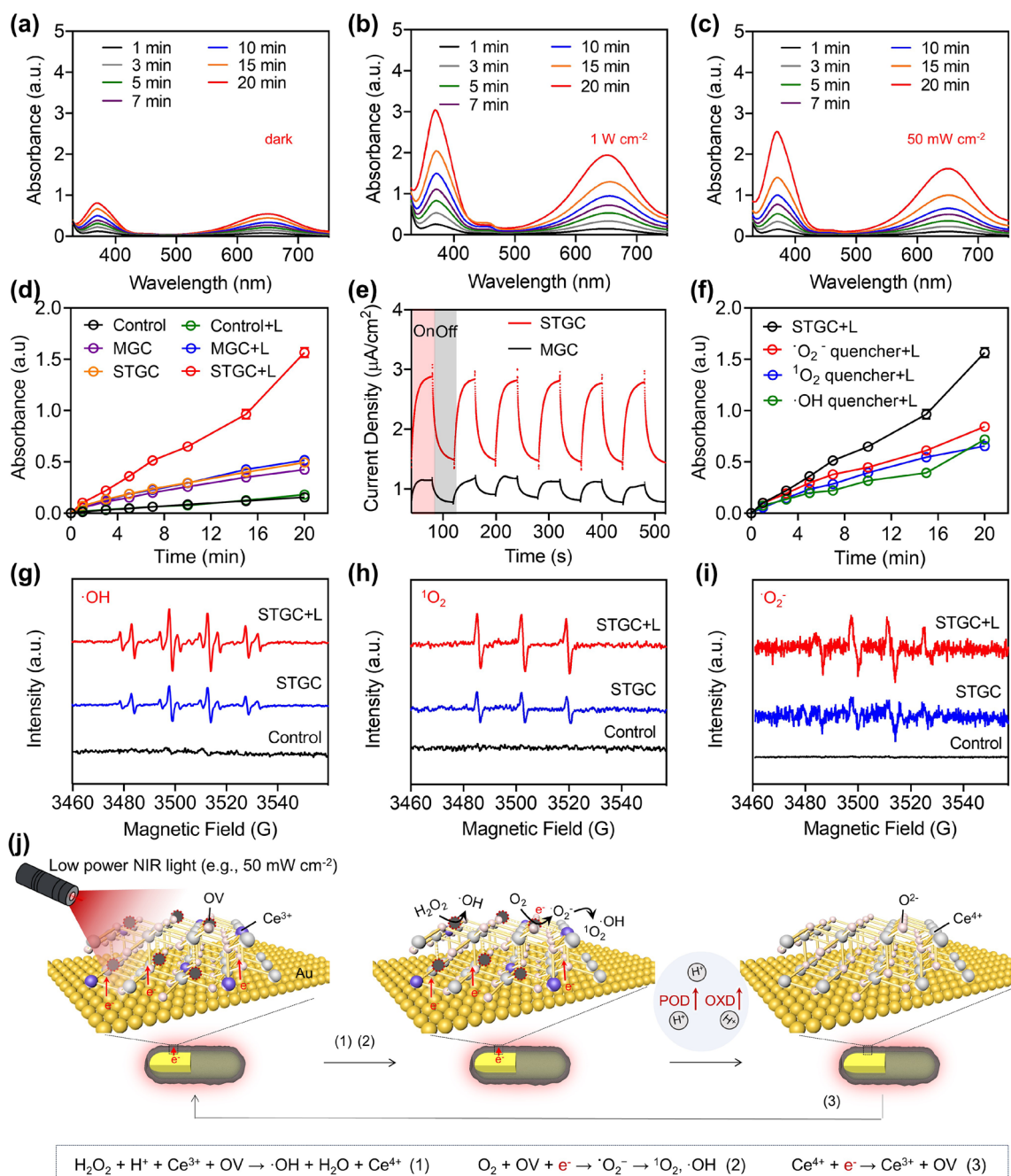
Fig. 2 Evaluation of the photocatalytic activity regulation of photon-driven sub-nanostructural transformable nanozymes. **a–c** TMB absorbance spectra upon the addition of STGC-PEG and H_2O_2 (10 mM) without (**a**), with 808 nm laser (1 W cm^{-2}) (**b**) or low-power 808 nm laser (50 mW cm^{-2}) irradiation (**c**). STGC denotes STGC-PEG. **d** Time-course absorbance of TMB oxidation product at 650 nm upon the addition of STGC-PEG or physical mixture of GNRs-PEG and CeO$_2$-PEG (MGC-PEG) with or without low-power 808 nm laser irradiation (50 mW cm^{-2}) in the presence of H_2O_2 (10 mM). MGC denotes MGC-PEG. Data are presented as means ± s.d. ($n=3$/group). **e** Electrochemical performances of STGC-PEG and MGC-PEG measured by *i–t* curve via a 808 nm laser ON–OFF switch (measured in 0.5 M H_2SO_4, 15 mV vs. Ag/AgCl). **f** Time-course absorbance of TMB oxidation products at 650 nm with different scavengers irradiated with low-power 808 nm laser (50 mW cm^{-2}). Data are presented as means ± s.d. ($n=3$/group). **g** ESR spectra of DMPO-OH spin adducts generated by STGC-PEG with or without low-power 808 nm laser irradiation (50 mW cm^{-2}, 5 min) in the presence of H_2O_2 (10 mM). **h, i** ESR spectra of TEMP-$^1O_2$ (**h**), and BMPO-$\cdot O_2^-$ (**i**) spin adducts generated by STGC-PEG with or without low-power 808 nm laser irradiation (50 mW cm^{-2}, 5 min). **j** Schematic illustration of atomic-level photon-mediated sub-nanostructural transformation of STGC-PEG for enzymatic activity regulation. Upon NIR irradiation, the generated hot electrons from Au can convert CeO$_2$ to CeO$_{2-x}$ and generate active OVs, thus endowing STGC-PEG with photon-promoted peroxidase (POD)- and oxidase (OXD)-like activities

via allosteric nanozymes for precisely controllable ROS-based nanomedicines.

2 Experimental and Calculation

2.1 Synthesis of STGC

The CTAB-capped GNRs were synthesized by the typical seed-mediated method [40]. $NaBH_4$ (10 mM, 50 μL) was injected into a mixture containing CTAB (0.1 M, 1.95 mL) and $HAuCl_4$ (10 mM, 50 μL) and stirred for 2 min to obtain the seed solution, which was placed at 27 °C for 2 h before use. For the preparation of growth solution, $HAuCl_4$ (10 mM, 15 mL), $AgNO_3$ (4 mM, 7.5 mL), AA (0.1 M, 1.2 mL) and the seed solution (450 μL) were injected into CTAB (0.1 M, 300 mL), and the solution was stirred for 2 min and then kept undisturbed at 27 °C at least 3 h. The final product was collected by centrifugation at 10,000 rpm for 15 min and re-dispersed into deionized water (DI water) as the stock solution (0.4 nM). STGC was synthesized through a modified solvothermal method [39]. For the preparation of STGC, CTAB (0.2 M, 1.125 mL), $EDTA-NH_3$ (10 mM, 0.35 mL) and $CeCl_3$ (0.1 M, 0.035 mL) were sequentially added into the GNRs stock solution (8 mL). Then, the solution was kept at 90 °C for 1.5 h in an oven. The final product was centrifuged and re-dispersed into DI water (2 mL) for further use.

2.2 Synthesis of Alendronate-Conjugated mPEG_{5K} (mPEG_{5K}-ALN)

$mPEG_{5K}$-ALN was synthesized according to the reported method by Yang et al. [41]. Briefly, $mPEG_{5K}$-COOH (500 mg), EDC (30 mg), and NHS (15 mg) were dissolved into DI water (4 mL) and stirred for 30 min. Then, alendronate sodium trihydrate (100 mg) and Na_2CO_3 (40 mg) were dissolved in DI water (2 mL) and added to the above solution. The reaction was carried out for 24 h, followed by dialysis and freeze-drying before collecting the final product.

2.3 Surface Modification of STGC

STGC (70 μg mL^{-1}, 2 mL), $mPEG_{5K}$-SH (10 mg), and $mPEG_{5K}$-ALN (30 mg) were mixed in 2 mL DI water for the ligand exchange process, and the mixture was stirred at room temperature (RT) for 24 h. The resulting PEGylated

STGC was isolated via centrifugation and rinsed three times with DI water for further use.

3 Results and Discussion

3.1 Synthesis of STGC

Ultrafine CeO_2 NPs were assembled on the surface of GNRs (Fig. S1) through a modified solvothermal method [39] to form well-dispersed STGC (Figs. 1b and S2-S3). Energy-dispersive spectrum (EDS) (Fig. S4a), line-scanning EDS (Fig. S4b), and elemental mapping (Fig. 1c) illustrate the distribution of Ce and O on the surface of GNRs. The mass ratio of Au: Ce in STGC is ~ 3: 1 as measured via inductively coupled plasma mass spectrometry (ICP-MS), where the relatively high Au-to-Ce ratio guarantees the sufficient hot electrons supply from Au and further photon-driven sub-nanostructural transformation of STGC. High-resolution transmission electron microscopy (HRTEM) (Fig. 1d) and X-ray diffraction (XRD) (Fig. 1e) pattern reveal the (111) plane of the fluorite cubic CeO_2 phase and the (111) plane of cubic Au phase, demonstrating the poly-crystalline nature of STGC. Besides, the red-shift of longitudinal surface plasmon resonance (LSPR) peak further suggests the successful coating of CeO_2 on GNRs, owning to the CeO_2 coating-induced local increase of refractive index, where strong NIR adsorption endows STGC with potential photo-triggered catalytic activity [39] (Fig. 1f). Moreover, X-ray photoelectron spectroscopy (XPS) spectrum reveals the coexistence of Ce^{3+} and Ce^{4+} in STGC (Fig. S5), suggesting the presence of OVs that maintain the charge balance [5, 38]. For further biomedical applications, the STGC was modified with poly(ethylene glycol) (PEG) (Fig. 1g), and the PEGylated STGC (STGC-PEG) with an average hydrodynamic diameter of ~ 128.5 nm (Fig. 1g, inset) and a negative charge (Fig. S6), is highly stable in water (Fig. S7). The successful PEGylation was further confirmed by XPS and Fourier transform infrared (FT-IR) (Fig. S8).

3.2 Photon-Driven Electron Transfer-Mediated Sub-Nanostructural Transformation

To verify the photon-driven electron transfer-mediated sub-nanostructural transformation of STGC, cyclic voltammetry (CV) curves of STGC were initially recorded. The

symmetrical redox peaks at around $+0.51$ and $+0.35$ V are assigned to the redox of Ce^{3+}/Ce^{4+} in CeO_2 [42, 43]; upon NIR irradiation, a significant peak current enhancement of STGC can be observed (Fig. 1h). The electric current enhancement agrees well with the proposal that the plasmon-excited hot electrons overcome the Schottky barrier and then transfer from Au to CeO_2 [39, 44], leading to the generation of Ce^{3+} and active OVs [42, 45, 46]. Intriguingly, the increase in electric current also occurred in H_2O_2-pretreated STGC (Fig. 1i). Besides, the regeneration of Ce^{3+} and OVs of CeO_2 NPs in the presence of H_2O_2 would be inhibited in acidic conditions [38, 47]. Therefore, the regeneration ability of CeO_2 NPs in STGC can be restored, benefiting from the electron transfer from Au to CeO_2 upon laser irradiation. Consistently, the LSPR peak of STGC red-shifts ($Ce^{3+} \rightarrow Ce^{4+}$) after co-incubation with H_2O_2 in acidic condition [39] and returns upon laser irradiation (Fig. S9). Moreover, as shown in Raman spectra (Fig. 1j), the initial 455 cm^{-1} peak (a symmetric breathing mode of oxygen atoms surrounding Ce ions [47, 48]) diminishes and a new peak at ~ 837 cm^{-1} (O–O stretching vibration of the absorbed peroxide species [49]) is observed after co-incubation with H_2O_2 in acidic condition, which can also be recovered after laser (L) irradiation. Furthermore, XPS and electron spin resonance (ESR) results manifest the formation of OVs in H_2O_2-treated STGC after laser irradiation (Fig. S10a-b), while the XRD patterns show that the crystal planes of CeO_2 (JCPDS No. 034-0394) do not reveal a significant change after reaction, indicating the light-mediated tunable catalytic activities are not based on the change of crystal planes (Fig. S10c). Impressively, more lattice disorder and dislocation upon laser irradiation are directly verified for H_2O_2-treated STGC by using atomic-resolution high-angle annular dark-field scanning transmission electron microscopy (HAADF-STEM) (Fig. 1k, l), which indicates the existence of numerous vacancies for the induction of coordinatively unsaturated metal atoms [50, 51], demonstrating the photon-driven sub-nanostructural transformation of STGC.

3.3 Photocatalytic Performance

We further investigated the photocatalytic performance of STGC-PEG. The oxidative activity of STGC-PEG sharply augments under high power (1 W cm^{-2}) NIR irradiation (Fig. 2a, b), which is significantly higher than that of the physical mixture of GNRs-PEG and CeO_2-PEG (MGC-PEG) (Figs. S11 and S12). More interestingly, the low-power (50 mW cm^{-2}) NIR irradiation that results in limited photothermal effect could also markedly trigger photocatalytic performance of STGC-PEG and leads to a three-fold increased oxidation of 3,3′,5,5′-tetramethylbenzidine (TMB) after 20 min (Fig. 2c, d). Besides, photocurrent measurements confirm the photon-driven electron transfer of STGC-PEG (Fig. 2e), which mediates sub-nanostructural transformation to enhance the oxidative activity. Moreover, the photon-augmented ROS are identified to be ·OH, $^1O_2$, and $\cdot O_2^-$ by using specific quenchers via UV–Vis and trapping agents via ESR analysis (Figs. 2f–i and S13), indicating photon-enhanced POD- and OXD-like activities of STGC-PEG. Specifically, extra H^+ may retard the reduction of Ce^{4+} and thus inhibit the decomposition of absorbed H_2O_2 [38, 47, 52], showing a restricted POD-like activity of STGC-PEG (Fig. S14). However, upon NIR irradiation, the interband transition of Au is excited to produce electron–hole pairs, and the hot electrons transfer from excited Au to the conduction band (CB) of CeO_2 to participate in the reduction of Ce^{4+} and produce active OVs, rebuilding the POD-like activity of STGC-PEG for H_2O_2 decomposition. Meanwhile, the active OVs can effectively trap the photogenerated hot electrons and O_2 [53, 54], significantly boosting the OXD-like activity to generate toxic $\cdot O_2^-/{}^1O_2/\cdot OH$ [46, 55–60] (Fig. 2j). Besides, the plasmon-excited holes on Au possess the oxidation ability and thus can drive the oxygen-evolution half-reaction ($2H_2O + 4$ $h^+ \rightarrow O_2 + 4H^+$), facilitating ROS generation as well as the equilibrium of electrons on the surface of Au [44, 61–63].

3.4 Low-Power NIR Light-Activated Tumor PCT

The photocatalytic effect of STGC-PEG was further investigated at the cellular level. STGC-PEG can be effectively internalized by 4T1 tumor cells (Figs. S15 and S16) without inducing noticeable dark cytotoxicity (Fig. 3a). Moreover, despite that GNRs-PEG show a photothermal conversion efficiency (η, 39.7%) comparable to that of STGC-PEG (37.2%; Fig. S17), only STGC-PEG shows significant cytotoxicity upon low-power NIR irradiation (50 mW cm^{-2}), which decreases the cellular viability to 59.7% at the concentration of 25 μg mL^{-1} Au (Fig. 3a, b), with the most severe ROS generation (Fig. 3c), mitochondrial damage (Fig. 3d)
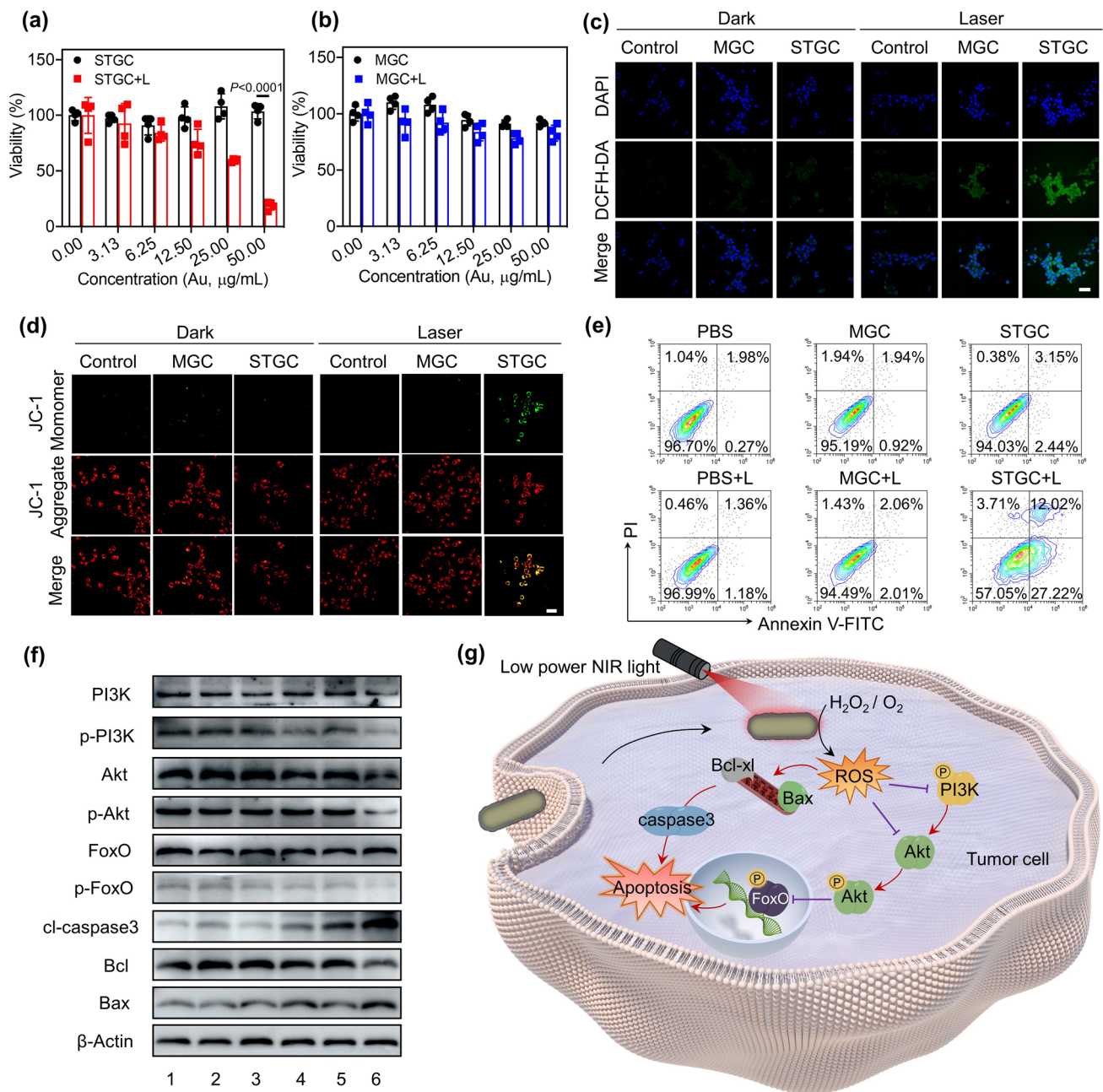
Fig. 3 In vitro photocatalytic therapy using photon-driven sub-nanostructural transformable nanozymes. **a** Cellular toxicity profile of STGC-PEG without or with 808 nm laser irradiation (50 mW cm^{-2}, 5 min). STGC denotes STGC-PEG. Data are presented as means±s.d. ($n=4$/group). **b** Cellular toxicity profile of MGC-PEG without or with 808 nm laser irradiation (50 mW cm^{-2}, 5 min). MGC denotes MGC-PEG. Data are presented as means±s.d. ($n=4$/group). **c** Fluorescence microscopy images of intracellular ROS levels in MGC-PEG- and STGC-PEG-treated 4T1 tumor cells without or with 808 nm laser irradiation (50 mW cm^{-2}, 5 min). Scale bar, 40 μm. **d** Fluorescence microscopy images of mitochondrial membrane potential in MGC-PEG- and STGC-PEG-treated 4T1 tumor cells without or with 808 nm laser irradiation (50 mW cm^{-2}, 5 min). The mitochondrial damage is indicated by the green fluorescent signals. Scale bar, 40 μm. **e** Flow cytometry analysis of cell apoptosis of MGC-PEG- and STGC-PEG-treated groups without or with 808 nm laser irradiation (50 mW cm^{-2}, 5 min). **f** Western blotting analysis of PI3k-Akt-FoXO signaling pathway and apoptosis-related proteins (1, PBS; 2, MGC-PEG; 3, STGC-PEG; 4, PBS+L; 5, MGC-PEG+L; 6, STGC-PEG+L). **g** Schematic illustration of ROS amplification and signaling pathways induced by photon-driven sub-nanostructural transformation of STGC-PEG
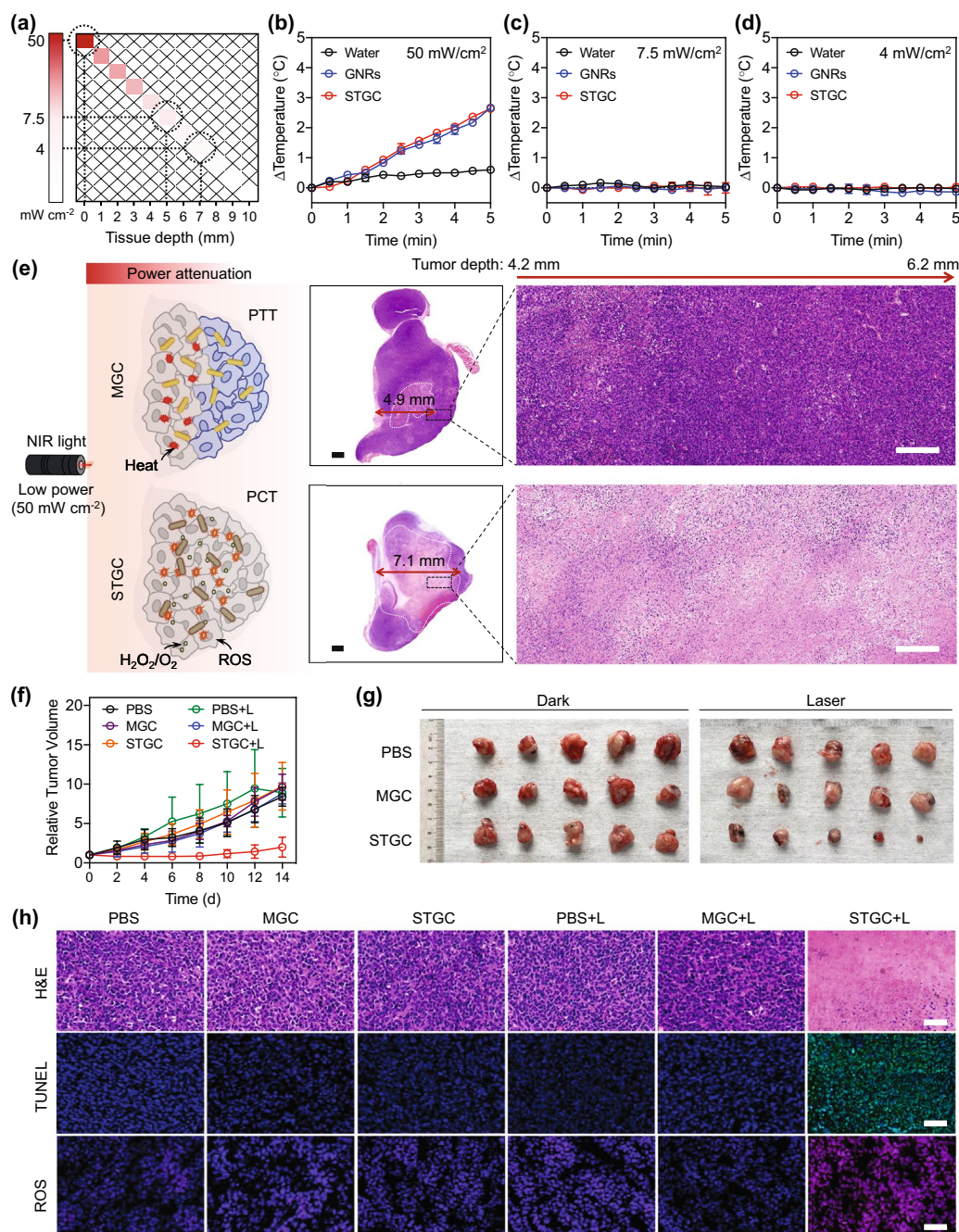
Fig. 4 In vivo photocatalytic therapy using photon-driven sub-nanostructural transformable nanozymes. **a** The attenuation of NIR light as it passes through tissues. Data are presented as means ± s.d. ($n = 3$/group). **b-d** The change of temperature generated by water, GNRs-PEG, and STGC-PEG (0.6 mg ml^{-1}, Au) under different NIR light power densities of 50 mW cm^{-2} (**b**), 7.5 mW cm^{-2} (**c**), and 4 mW cm^{-2} (**d**) for 5 min, which are corresponding to the power attenuation at tissue thickness of 0 mm, 5 mm, and 7 mm, respectively. STGC denotes STGC-PEG, and GNRs denote GNRs-PEG. Data are presented as means ± s.d. ($n = 3$/group). **e** The schematic illustration and H&E staining of the whole tumors of the mice after the treatments of MGC-PEG-mediated power-dependent PTT and STGC-PEG-mediated deep tumor PCT upon the attenuated laser irradiation. Scale bars, 1 mm (left) and 200 μm (right). STGC-PEG + L leads to a greater tumor necrosis depth (~7.1 mm) as compared to MGC-PEG + L (~4.9 mm). MGC denotes MGC-PEG. **f** 4T1-tumor growth curves of the mice with different treatments measured every other day. Data are presented as means ± s.d. ($n = 5$/group). **g** Photograph of tumors on the 14th day after various treatments without or with 808 nm laser irradiation (50 mW cm^{-2}, 5 min). **h** H&E, TUNEL, and ROS staining of tumor tissues in different groups. STGC-PEG + L-treated group exhibits the most shrunken nucleus (in H&E staining), the highest cell apoptosis ratio (the TUNEL positive cells are indicated by the green fluorescent signals), and the highest ROS level (indicated by the increased red fluorescence intensity). Scale bar, 50 μm

and apoptosis rate of tumor cells (Fig. 3e). Besides, STGC-PEG displays a much lower cytotoxicity on human normal cell lines including hepatic cell L02 and colonic epithelial cell NCM460 even upon NIR irradiation, probably resulting from the relatively low level of H_2O_2 in normal cells (Fig. S18). Taken together, we conclude that upon internalization into tumor cells, the conversion from CeO_2 to electron-rich state of CeO_{2-x} as well as the active OVs generation would be initiated by the hot-electron injection from gold to ceria upon low-power NIR irradiation, whereafter the dynamic sub-nanostructural transformation of STGC-PEG triggers the excess ROS generation for effective tumor cell killing.

Furthermore, we examined the changes in the molecular pathway of 4T1 tumor cells after different treatments. As shown in Fig. 3f, the levels of Akt, phosphorylated Akt (p-Akt), p-PI3K and p-FoxO, which are well implicated in breast cancer development, are downregulated by STGC-PEG upon NIR irradiation. Moreover, STGC-PEG induces the downregulation of antiapoptotic Bcl-xl, the upregulation of proapoptotic Bax and cleaved caspase-3 (cl-caspase-3) during the PCT. Consequently, we reason that the toxic ROS generated by STGC-PEG not only directly affect Bcl-2 family proteins and activate pro-apoptotic pathways [64], but also inhibit the PI3K/Akt/FoxO signaling cascade, thus promoting the tumor cell death (Fig. 3g).

Encouraged by in vitro results, we further evaluated the in vivo tumor PCT using STGC-PEG under low-power NIR irradiation (50 mW cm^{-2}). Considering that high light fluency can inevitably induce the necrosis of the normal tissues [65, 66], it is appealing to achieve potent phototherapy with minimal light intensity, especially for deep-seated tumors requiring light penetration through tissue barriers that diminish light intensity at the tumor sites. Due to the power attenuation in thick biological tissues, the power density of laser sharply declines as measured by a power meter, for example, by 85.1% and 92.2% at tissue thickness of 5 mm and 7 mm, respectively (Fig. 4a–d). Interestingly, because of the sharp NIR light attenuation in deep tumor tissues, through hematoxylin and eosin (H&E) staining of the whole tumor after the laser irradiation, we find that MGC-PEG leads to limited tumor necrosis due to the power-dependent photothermal effect, while STGC-PEG induces severe tumor necrosis with a much larger area and greater depth (Fig. 4e). This finding strengthens the advantage of the low-power NIR irradiation-triggered deep tumor PCT by using STGC-PEG via the markedly high-performance photon-mediated sub-nanostructural transformation.

Consequently, STGC-PEG effectively suppresses the progression of 4T1 breast cancer, while MGC-PEG shows no obvious tumor growth inhibition (Figs. 4f–g and S19). Furthermore, the ROS level in STGC-PEG + laser-treated tumor presents to be the highest among all the groups, indicating the highly efficient in situ photocatalytic reaction. H&E and terminal deoxynucleotidyl transferase dUTP nick end label (TUNEL) staining results reveal not only significantly severe cell apoptosis, but also markedly deep tumor destruction in STGC-PEG + L group (Fig. 4h). Notably, similar to control group, neither obvious body weight change (Fig. S20), nor noticeable pathological tissue damage or abnormality from the histology analysis (H&E staining) (Fig. S21) can be found in mice treated with STGC-PEG. Besides, body weights (Fig. S22), serum biochemical analysis (Fig. S23), hematological index (Fig. S24), as well as H&E staining (Fig. S25) of healthy normal BALB/c mice all demonstrate the great biocompatibility of STGC-PEG in vivo. To our best knowledge, this is the first demonstration of a nanozyme that, by virtue of the dynamic sub-nanostructural transformation-mediated catalytic activity regulation, can achieve excellent low-power NIR light-activated photocatalytic ablation of tumors in vivo; such a sub-nanostructural transformable nanozyme enabled tumor PCT is superior to conventional light-mediated therapies, such as PTT and photodynamic therapy, whose efficacy can be significantly affected by light attenuation in tissues or tumor hypoxia.

4 Conclusions

We have developed a photon-driven sub-nanostructural transformable nanozyme (STGC-PEG) with light-responsive sub-nanostructural transformation that can fine-tune its catalytic activities in biological environment. Upon NIR irradiation, the plasmon-excited hot electrons transfer from Au to CeO_2 to initiate CeO_2–CeO_{2-x} conversion and generate active OVs, endowing STGC-PEG with dramatically amplified POD- and OXD-like activities. Importantly, STGC-PEG results in massive augmentation of ROS production with spatiotemporal controllability upon low-power NIR irradiation and thus potentiate the anti-tumor efficiency of PCT both in vitro and in vivo. Particularly, for the first time, STGC-PEG successfully achieves excellent low power NIR light-activated photocatalytic ablation of tumors in vivo. As a proof-of-concept, our strategy provides a new paradigm for fabricating dynamically transformable nanozyme

with tunable catalytic performances in vivo for biomedical applications. Our findings may aid the future design of advanced biomimetic nanocatalysts and provide a model for approaching natural enzyme-like activity control of artificial nanozymes.

Supplementary Information The online version contains supplementary material available at https://doi.org/10.1007/s40820-022-00848-y.

References

1. P. Srinivasan, C.D. Smolke, Biosynthesis of medicinal tropane alkaloids in yeast. Nature **585**(7826), 614–619 (2020). https://doi.org/10.1038/s41586-020-2650-9

2. J.C. Ullman, A. Arguello, J.A. Getz, A. Bhalla, C.S. Mahon et al., Brain delivery and activity of a lysosomal enzyme using a blood-brain barrier transport vehicle in mice. Sci. Transl. Med. **12**(545), eaay1163 (2020). https://doi.org/10.1126/scitranslmed.aay1163

3. Y. Huang, J. Ren, X. Qu, Nanozymes: classification, catalytic mechanisms, activity regulation, and applications. Chem. Rev. **119**(6), 4357–4412 (2019). https://doi.org/10.1021/acs.chemrev.8b00672

4. Y. Li, J. Liu, Nanozyme's catching up: activity, specificity, reaction conditions and reaction types. Mater. Horiz. **8**(2), 336–350 (2021). https://doi.org/10.1039/D0MH01393E

5. T. Kang, Y.G. Kim, D. Kim, T. Hyeon, Inorganic nanoparticles with enzyme-mimetic activities for biomedical applications. Coordin. Chem. Rev. **403**, 213092 (2020). https://doi.org/10.1016/j.ccr.2019.213092

6. S. Li, L. Shang, B. Xu, S. Wang, K. Gu et al., A nanozyme with photo-enhanced dual enzyme-like activities for deep pancreatic cancer therapy. Angew. Chem. Int. Ed. **58**(36), 12624–12631 (2019). https://doi.org/10.1002/ange.201904751

7. S. Zhao, M. Riedel, J. Patarroyo, N. Bastus, V. Puntes et al., Introducing visible-light sensitivity into photocatalytic CeO$_2$ nanoparticles by hybrid particle preparation exploiting plasmonic properties of gold: enhanced photoelectrocatalysis exemplified for hydrogen peroxide sensing. Nanoscale **13**(2), 980–990 (2021). https://doi.org/10.1039/D0NR06356H

8. W. Zhen, Y. Liu, W. Wang, M. Zhang, W. Hu et al., Specific "unlocking" of a nanozyme-based butterfly effect to break the evolutionary fitness of chaotic tumors. Angew. Chem. Int. Ed. **59**(24), 9491–9497 (2020). https://doi.org/10.1002/ange.201916142

9. G. Tang, J. He, J. Liu, X. Yan, K. Fan, Nanozyme for tumor therapy: surface modification matters. Exploration **1**, 75–89 (2021). https://doi.org/10.1002/EXP.20210005

10. B. Das, J. Franco, N. Logan, P. Balasubramanian, M. Kim et al., Nanozymes in point-of-care diagnosis: an emerging futuristic approach for biosensing. Nano-Micro Lett. **13**, 193 (2021). https://doi.org/10.1007/s40820-021-00717-0

11. J. Wu, X. Wang, Q. Wang, Z. Lou, S. Li et al., Nanomaterials with enzyme-like characteristics (nanozymes): next-generation artificial enzymes (II). Chem. Soc. Rev. **48**(4), 1004–1076 (2019). https://doi.org/10.1039/C8CS00457A

12. Y. Liu, Y. Cheng, H. Zhang, M. Zhou, Y. Yu et al., Integrated cascade nanozyme catalyzes in vivo ROS scavenging for anti-inflammatory therapy. Sci. Adv. **6**(29), eabb2695 (2020). https://doi.org/10.1126/sciadv.abb2695

13. K. Fan, J. Xi, L. Fan, P. Wang, C. Zhu et al., In vivo guiding nitrogen-doped carbon nanozyme for tumor catalytic therapy. Nat. Commun. **9**, 1440 (2018). https://doi.org/10.1038/s41467-018-03903-8

14. T. Liu, B. Xiao, F. Xiang, J. Tan, Z. Chen et al., Ultrasmall copper-based nanoparticles for reactive oxygen species scavenging and alleviation of inflammation related diseases. Nat. Commun. **11**, 2788 (2020). https://doi.org/10.1038/s41467-020-16544-7

15. F. Wang, E. Ju, Y. Guan, J. Ren, X. Qu, Light-mediated reversible modulation of ROS level in living cells by using an activity-controllable nanozyme. Small **13**(25), 1603051 (2017). https://doi.org/10.1002/smll.201603051

16. F. Wang, Y. Zhang, Z. Du, J. Ren, X. Qu, Designed heterogeneous palladium catalysts for reversible light-controlled

bioorthogonal catalysis in living cells. Nat. Commun. **9**, 1209 (2018). https://doi.org/10.1038/s41467-018-03617-x

17. D. Jiang, D. Ni, Z.T. Rosenkrans, P. Huang, X. Yan et al., Nanozyme: new horizons for responsive biomedical applications. Chem. Soc. Rev. **48**(14), 3683–3704 (2019). https://doi.org/10.1039/C8CS00718G

18. H. Ye, K. Yang, J. Tao, Y. Liu, Q. Zhang et al., An enzyme-free signal amplification technique for ultrasensitive colorimetric assay of disease biomarkers. ACS Nano **11**(2), 2052–2059 (2017). https://doi.org/10.1021/acsnano.6b08232

19. M. Huo, L. Wang, Y. Chen, J. Shi, Tumor-selective catalytic nanomedicine by nanocatalyst delivery. Nat. Commun. **8**, 357 (2017). https://doi.org/10.1038/s41467-017-00424-8

20. K. Xu, Y. Cheng, J. Yan, Y. Feng, R. Zheng et al., Polydopamine and ammonium bicarbonate coated and doxorubicin loaded hollow cerium oxide nanoparticles for synergistic tumor therapy. Nano Res. **12**(12), 2947–2953 (2019). https://doi.org/10.1007/s12274-019-2532-3

21. T. Pan, Y. Wang, X. Xue, C. Zhang, Rational design of allosteric switchable catalysts. Exploration (2022). https://doi.org/10.1002/EXP.20210095

22. M. Wegener, M.J. Hansen, A.J. Driessen, W. Szymanski, B.L. Feringa et al., Photocontrol of antibacterial activity: shifting from UV to red light activation. J. Am. Chem. Soc. **139**(49), 17979–17986 (2017). https://doi.org/10.1021/jacs.7b09281

23. K. Singh, B. Graf, A. Linden, V. Sautner, H. Urlaub et al., Discovery of a regulatory subunit of the yeast fatty acid synthase. Cell **180**(6), 1130–1143 (2020). https://doi.org/10.1016/j.cell.2020.02.034

24. J. Kuriyan, D. Eisenberg, The origin of protein interactions and allostery in colocalization. Nature **450**(7172), 983–990 (2007). https://doi.org/10.1038/nature06524

25. M.J. Comstock, K.D. Whitley, H. Jia, J. Sokoloski, T.M. Lohman et al., Direct observation of structure-function relationship in a nucleic acid-processing enzyme. Science **348**(6232), 352–354 (2015). https://doi.org/10.1126/science.aaa0130

26. R. Szmola, M. Sahin-Tóth, Pancreatitis-associated chymotrypsinogen C (CTRC) mutant elicits endoplasmic reticulum stress in pancreatic acinar cells. Gut **59**(3), 365–372 (2010). https://doi.org/10.1136/gut.2009.198903

27. O. Berntsson, R. Rodriguez, L. Henry, M.R. Panman, A.J. Hughes et al., Photoactivation of drosophila melanogaster cryptochrome through sequential conformational transitions. Sci. Adv. **5**(7), eaaw1531 (2019). https://doi.org/10.1126/sciadv.aaw1531

28. R. Nussinov, C.J. Tsai, Allostery in disease and in drug discovery. Cell **153**(2), 293–305 (2013). https://doi.org/10.1016/j.cell.2013.03.034

29. H.G. Saavedra, J.O. Wrabl, J.A. Anderson, J. Li, V.J. Hilser, Dynamic allostery can drive cold adaptation in enzymes. Nature **558**(7709), 324–328 (2018). https://doi.org/10.1038/s41586-018-0183-2

30. U. Aslam, V.G. Rao, S. Chavez, S. Linic, Catalytic conversion of solar to chemical energy on plasmonic metal nanostructures. Nat. Catal. **1**(9), 656–665 (2018). https://doi.org/10.1038/s41929-018-0138-x

31. M. Ha, J.H. Kim, M. You, Q. Li, C. Fan et al., Multicomponent plasmonic nanoparticles: from heterostructured nanoparticles to colloidal composite nanostructures. Chem. Rev. **119**(24), 12208–12278 (2019). https://doi.org/10.1021/acs.chemrev.9b00234

32. Y. Chang, Y. Cheng, Y. Feng, H. Jian, L. Wang et al., Resonance energy transfer-promoted photothermal and photodynamic performance of gold-copper sulfide yolk-shell nanoparticles for chemophototherapy of cancer. Nano Lett. **18**(2), 886–897 (2018). https://doi.org/10.1021/acs.nanolett.7b04162

33. S.S. Wang, L. Jiao, Y. Qian, W.C. Hu, G.Y. Xu et al., Boosting electrocatalytic hydrogen evolution over metal-organic frameworks by plasmon-induced hot-electron injection. Angew. Chem. Int. Ed. **58**(31), 10713–10717 (2019). https://doi.org/10.1002/ange.201906134

34. L. Wang, X. Xu, Q. Cheng, S.X. Dou, Y. Du, Near-infrared-driven photocatalysts: design, construction, and applications. Small **17**(9), 1904107 (2019). https://doi.org/10.1002/smll.201904107

35. B.H. Lee, S. Park, M. Kim, A.K. Sinha, S.C. Lee et al., Reversible and cooperative photoactivation of single-atom Cu/TiO$_2$ photocatalysts. Nat. Mater. **18**(6), 620–626 (2019). https://doi.org/10.1038/s41563-019-0344-1

36. Y. Li, X. He, J. Yin, Y. Ma, P. Zhang et al., Acquired superoxide-scavenging ability of ceria nanoparticles. Angew. Chem. Int. Ed. **54**(6), 1832–1835 (2015). https://doi.org/10.1002/anie.201410398

37. G.H. Ryu, A. France-Lanord, Y. Wen, S. Zhou, J.C. Grossman et al., Atomic structure and dynamics of self-limiting sub-nanometer pores in monolayer WS$_2$. ACS Nano **12**(11), 11638–11647 (2018). https://doi.org/10.1021/acsnano.8b07051

38. C. Xu, X. Qu, Cerium oxide nanoparticle: a remarkably versatile rare earth nanomaterial for biological applications. NPG Asia Mater. **6**, e90 (2014). https://doi.org/10.1038/am.2013.88

39. B. Li, T. Gu, T. Ming, J. Wang, P. Wang et al., (Gold core)@(ceria shell) nanostructures for plasmon-enhanced catalytic reactions under visible light. ACS Nano **8**(8), 8152–8162 (2014). https://doi.org/10.1021/nn502303h

40. B. Nikoobakht, M.A. El-Sayed, Preparation and growth mechanism of gold nanorods (NRs) using seed-mediated growth method. Chem. Mater. **15**(10), 1957–1962 (2003). https://doi.org/10.1021/cm0207321

41. Z.Y. Yang, S.L. Luo, H. Li, S.W. Dong, J. He et al., Alendronate as a robust anchor for ceria nanoparticle surface coating: facile binding and improved biological properties. RSC Adv. **4**(104), 59965–59969 (2014). https://doi.org/10.1039/C4RA12007H

42. Y. Zhao, Y. Wang, A. Mathur, Y. Wang, V. Maheshwari et al., Fluoride-capped nanoceria as a highly efficient oxidase-mimicking nanozyme: inhibiting product adsorption and increasing

oxygen vacancies. Nanoscale **11**(38), 17841–17850 (2019). https://doi.org/10.1039/C9NR05346H

43. T. Saravanan, M. Shanmugam, P. Anandan, M. Azhagurajan, K. Pazhanivel et al., Facile synthesis of graphene-CeO$_2$ nanocomposites with enhanced electrochemical properties for supercapacitors. Dalton Trans. **44**(21), 9901–9908 (2015). https://doi.org/10.1039/C5DT01235J

44. X. Guo, X. Li, S. Kou, X. Yang, X. Hu et al., Plasmon-enhanced electrocatalytic hydrogen/oxygen evolution by Pt/Fe-Au nanorods. J. Mater. Chem. A **6**(17), 7364–7369 (2018). https://doi.org/10.1039/C8TA00499D

45. Y. Temerk, H. Ibrahim, A new sensor based on In doped CeO$_2$ nanoparticles modified glassy carbon paste electrode for sensitive determination of uric acid in biological fluids. Sens. Actuators B Chem. **224**, 868–877 (2016). https://doi.org/10.1016/j.snb.2015.11.029

46. C.T. Campbell, C.H. Peden, Oxygen vacancies and catalysis on ceria surfaces. Science **309**(5735), 713–714 (2005). https://doi.org/10.1126/science.1113955

47. Y.J. Wang, H. Dong, G.M. Lyu, H.Y. Zhang, J. Ke et al., Engineering the defect state and reducibility of ceria based nanoparticles for improved anti-oxidation performance. Nanoscale **7**(33), 13981–13990 (2015). https://doi.org/10.1039/C5NR02588E

48. D. Ni, H. Wei, W. Chen, Q. Bao, Z.T. Rosenkrans et al., Ceria nanoparticles meet hepatic ischemia-reperfusion injury: the perfect imperfection. Adv. Mater. **31**(40), 1902956 (2019). https://doi.org/10.1002/adma.201902956

49. F. Scholes, A. Hughes, S. Hardin, P. Lynch, P.R. Miller, Influence of hydrogen peroxide in the preparation of nanocrystalline ceria. Chem. Mater. **19**(9), 2321–2328 (2007). https://doi.org/10.1021/cm063024z

50. X. Sun, X. Luo, X. Zhang, J. Xie, S. Jin et al., Enhanced superoxide generation on defective surfaces for selective photooxidation. J. Am. Chem. Soc. **141**(9), 3797–3801 (2019). https://doi.org/10.1021/jacs.8b13051

51. N. Zhang, X. Li, H. Ye, S. Chen, H. Ju et al., Oxide defect engineering enables to couple solar energy into oxygen activation. J. Am. Chem. Soc. **138**(28), 8928–8935 (2016). https://doi.org/10.1021/jacs.6b04629

52. Z. Wang, X. Shen, X. Gao, Y. Zhao, Simultaneous enzyme mimicking and chemical reduction mechanisms for nanoceria as a bio-antioxidant: a catalytic model bridging computations and experiments for nanozymes. Nanoscale **11**(28), 13289–13299 (2019). https://doi.org/10.1039/c9nr03473k

53. J. Xiong, J. Di, J. Xia, W. Zhu, H. Li, Surface defect engineering in 2D nanomaterials for photocatalysis. Adv. Funct. Mater. **28**(39), 1801983 (2018). https://doi.org/10.1002/adfm.201801983

54. S.I. Han, S. Lee, M.G. Cho, J.M. Yoo, M.H. Oh et al., Epitaxially strained CeO$_2$/Mn$_3$O$_4$ nanocrystals as an enhanced antioxidant for radioprotection. Adv. Mater. **32**(31), 2001566 (2020). https://doi.org/10.1002/adma.202001566

55. A.M. Nauth, E. Schechtel, R. Dören, W. Tremel, T. Opatz, TiO$_2$ nanoparticles functionalized with non-innocent ligands allow oxidative photocyanation of amines with visible/

56. H. Zhu, Y. Fang, Q. Miao, X. Qi, D. Ding et al., Regulating near-infrared photodynamic properties of semiconducting polymer nanotheranostics for optimized cancer therapy. ACS Nano **11**(9), 8998–9009 (2017). https://doi.org/10.1021/acsnano.7b03507

57. G. Lan, K. Ni, S.S. Veroneau, X. Feng, G.T. Nash et al., Titanium-based nanoscale meta-organic framework for type I photodynamic therapy. J. Am. Chem. Soc. **141**(10), 4204–4208 (2019). https://doi.org/10.1021/jacs.8b13804

58. Z. Tian, J. Li, Z. Zhang, W. Gao, X. Zhou et al., Highly sensitive and robust peroxidase-like activity of porous nanorods of ceria and their application for breast cancer detection. Biomaterials **59**, 116–124 (2015). https://doi.org/10.1016/j.biomaterials.2015.04.039

59. L. Jiang, S. Fernandez-Garcia, M. Tinoco, Z. Yan, Q. Xue et al., Improved oxidase mimetic activity by praseodymium incorporation into ceria nanocubes. ACS Appl. Mater. Interfaces **9**(22), 18595–18608 (2017). https://doi.org/10.1021/acsami.7b05036

60. Z. Wang, X. Shen, X. Gao, Density functional theory mechanistic insight into the peroxidase- and oxidase-like activities of nanoceria. J. Phys. Chem. C **125**(42), 23098–23104 (2021). https://doi.org/10.1021/acs.jpcc.1c04878

61. X. Xu, S. Kou, X. Guo, X. Li, X. Ma et al., The enhanced photocatalytic properties for water oxidation over Bi/BiVO$_4$/V$_2$O$_5$ Composite. J. Phys. Chem. C **121**(30), 16257–16265 (2017). https://doi.org/10.1021/acs.jpcc.7b03119

62. S. Linic, P. Christopher, D.B. Ingram, Plasmonic-metal nanostructures for efficient conversion of solar to chemical energy. Nat. Mater. **10**(12), 911–921 (2011). https://doi.org/10.1038/NMAT3151

63. J. Wang, M. Chen, Z. Luo, L. Ma, Y. Zhang et al., Ceria-coated gold nanorods for plasmon-enhanced near-infrared photocatalytic and photoelectrochemical performances. J. Phys. Chem. C **120**(27), 14805–14812 (2016). https://doi.org/10.1021/acs.jpcc.6b03753

64. Y. Du, C. Yang, F. Li, H. Liao, Z. Chen et al., Core-shell-satellite nanomaces as remotely controlled self-fueling fenton reagents for imaging-guided triple-negative breast cancer-specific therapy. Small **16**(31), 2002537 (2020). https://doi.org/10.1002/smll.202002537

65. D. Ling, B. Bae, W. Park, K. Na, Photodynamic efficacy of photosensitizers under an attenuated light dose via lipid nano-carrier-mediated nuclear targeting. Biomaterials **33**(21), 5478–5486 (2012). https://doi.org/10.1016/j.biomaterials.2012.04.023

66. J. Li, X. Liu, L. Tan, Z. Cui, X. Yang et al., Zinc-doped Prussian blue enhances photothermal clearance of Staphylococcus aureus and promotes tissue repair in infected wounds. Nat. Commun. **10**, 4490 (2019). https://doi.org/10.1038/s41467-019-12429-6